remote sensing

MDPI

Article

Life Cycle Mining Deformation Monitoring and Analysis Using Sentinel-1 and Radarsat-2 InSAR Time Series

Zhi Ma [1], Xiaoqing Yang [2,*], Lei Xie [1] and Wei Dong [3]

[1] School of Geosciences and Info-Physics, Central South University, Changsha 410083, China; 225012193@csu.edu.cn (Z.M.); leixie_geo@csu.edu.cn (L.X.)
[2] Information & Network Center, Central South University, Changsha 410083, China
[3] China Railway Siyuan Survey and Design Group Co., Ltd., Wuhan 430063, China; tsygkydw@163.com
* Correspondence: 218168@csu.edu.cn

Abstract: The life cycle of mining results in various patterns of surface deformation as it progresses through development, production, and reclamation. Therefore, the spatial–temporal patterns of ground deformation provide a crucial indicator to understand the mining activities, related geohazards, and environmental restoration. This study investigates the decadal deformation (2012–2022) of three coal mines during different stages of mines' life cycles in Henan, China, using radar interferometry with Radarsat-2 and Sentinel-1 data. The results reveal multiple deformation patterns across different areas: the Changcun mine area changed from ground subsidence to uplift following the termination of exploitation in 2016; the Xiadian mine area has been continuously developing over the past decade, resulting in a cumulative subsidence of 55.6 mm; and the Liyuan mine area exhibits surface rebound at a rate of 7.9 mm/year since its closure in 2007. We also probe the mining geometry of the production process by using a rectangular model. This study highlights the significance of long-term InSAR observations and deformation modeling in elucidating the mining operation dynamics of small mining zones in their production, transition, and post-closure periods, thereby facilitating the management of small-scale mining.

Keywords: synthetic aperture radar interferometry; mine life cycle deformation; deformation modeling; Radarsat-2; Sentinel-1

Citation: Ma, Z.; Yang, X.; Xie, L.; Dong, W. Life Cycle Mining Deformation Monitoring and Analysis Using Sentinel-1 and Radarsat-2 InSAR Time Series. *Remote Sens.* **2024**, *16*, 2335. https://doi.org/10.3390/rs16132335

Academic Editor: Salvatore Stramondo

Received: 18 May 2024
Revised: 19 June 2024
Accepted: 21 June 2024
Published: 26 June 2024

1. Introduction

The closure of small and environmentally unfriendly coal mines is crucial for China's energy structure transition towards a low-carbon economy. Between 2006 and 2013, over 20,000 small coal mines were closed, with plans to terminate another 15,000 by 2030 in China [1]. However, the process of "mining, closure, and reclamation" in small coal mines (i.e., coal mines with annual production below 0.45 million tons per year) often spans several years to decades. Geological hazards such as surface subsidence, ground fissures, and sinkholes may continue to develop even after the termination of mining [2–4]. However, the decadal monitoring of surface deformation in mining areas and goafs remains challenging due to the high labor and economic costs of traditional in situ geodetic observations, impeding subsequent management and ecological restoration efforts in small-scale mining areas [5,6].

In recent decades, multi-temporal InSAR techniques (MT-InSAR), such as Persistent Scatterer InSAR (PS-InSAR) [7,8] and Small Baseline Subset InSAR (SBAS-InSAR) [9–11], have become popular for deformation monitoring and modeling in mining areas [12–17]. Several studies focus on the surface subsidence after coal mine closures [18–22]. For example, Guéguen et al. (2009) estimated surface displacement 15 years after the closure of coal mines in Nord/Pas-de-Calais, France, using D-InSAR and PS-InSAR. Their findings indicated that the surface deformation gradually stabilized in the post-closure period [23]. Jung et al. (2007) used JERS-1 SAR data from 1992 to 1998 to monitor subsidence in the

abandoned Gaeun coal mine in South Korea with PS-InSAR. The results showed an excellent agreement between the InSAR-estimated subsidence and in situ fissure distribution [24]. Zheng et al. (2023) demonstrated a four-stage change in post-closure surface deformation as "subsidence-stabilization-uplift-stabilization" in Xuzhou, China, from 2016–2019 Sentinel-1 data [25]. In Europe, several studies also reported that the groundwater level can change the surface deformation from InSAR observations. For example, Bejarano Urrego et al. (2016) showed that the abandoned Zolder mine in Belgium experienced an uplift of 5.6 mm/year, which was related to the rising groundwater [26]. Gee et al. (2017) reported a linear relationship between the surface uplift and groundwater level from the InSAR observations in Northumberland and Durham coal fields, UK [27]. Blachowski et al. (2018) indicated that a 12 mm/year ground uplift in Walbrzych Coal Basin, Poland may be caused by the increasing hydrostatic water pressure in the rock matrix and the corresponding stress redistributions [28].

These InSAR-based deformation measurements can also be used to probe the geometry and process of mining activities. He et al. (2022) used the multi-source Okada model, a dislocation model for shear and tensile fault motions in an elastic half-space [29], to simulate ground deformation obtained using the coherent scatterer InSAR technique. The results showed that the predicted and observed deformations were highly correlated, with an overall misfit of less than 5 cm [30]. Lu et al. (2013) modeled a mining area with vertical deformation by ignoring the deformation in strike-slip and dip-slip directions and assumed a horizontal tunnel in the Okada model for simplification. Their results showed a high degree of consistency between the leveling and model predictions [31]. Dai et al. (2020) used both the Okada and Mogi models to invert the D-InSAR-based surface deformation by the probability integral method in Huainan coalfield. They found that the more complex and adaptable Okada model performs better at a higher noise level [32]. Ren et al. (2021) also effectively monitored and reversed the deformation of the Dianping coal mine by combining the SBAS-InSAR technique with the dislocation [33].

However, most of the existing studies only capture and model the mining deformation in a short period (i.e., 3–5 years), which cannot cover the entire mining life cycle. Therefore, our understanding of the surface deformation patterns and mechanisms before and after coal mining cessation is still limited. In this study, we first combined Radarsat-2 and Sentinel-1 to achieve continuous monitoring from January 2012 to December 2022 in three mining areas in Henan, China. Second, we employed the rectangular dislocation model and Bayesian inversion method to probe the geometry parameters of the coal seam. Third, we discussed the deformation mechanisms during different stages of the mining life cycle.

2. Materials and Methods

2.1. Study Area

The study area is located in Luoyang and Pingdingshan, Henan, China. This area encompasses two tectonic units: the North China Craton and the Qinling Trough, which have experienced multiple stages of geological activity, leading to the formation of rocks. It hosts abundant mineral resources, including coal, iron, lead, and molybdenum, and has hosted mining operations for several decades. The study area has three primary mining regions (Figure 1a): (1) Longmen mine area has Longmen, Zhengxingsu, and Changcun coal mines (Figure 1b). The Longmen coal mine has been operated since January 2003, producing 0.5 million tons per year across an area of 5.7 km^2. The Changcun coal mine operated from July 2010 to September 2016, and it covers 18.9 km^2, with an annual production of 1.8 million tons. The Zhengxingsu coal mine operated from March 2011 to December 2021, with an annual coal production of 0.15 million tons over 1.08 km^2. (2) Xiadian coal mine is located in Pingdingshan City. The mine's capacity amounts to 195 million tons in an area of 26.4 km^2. It has been in continuous operation since May 2010, with an annual coal production capacity of 1.5 million tons. (3) Liyuan coal mine is 17.2 km south of the Xiadian coal mine. The operation lasted for 17 years from December 1990 to September

2007, with an annual production of 0.45 million tons. And the mining style here is longwall mining [34].

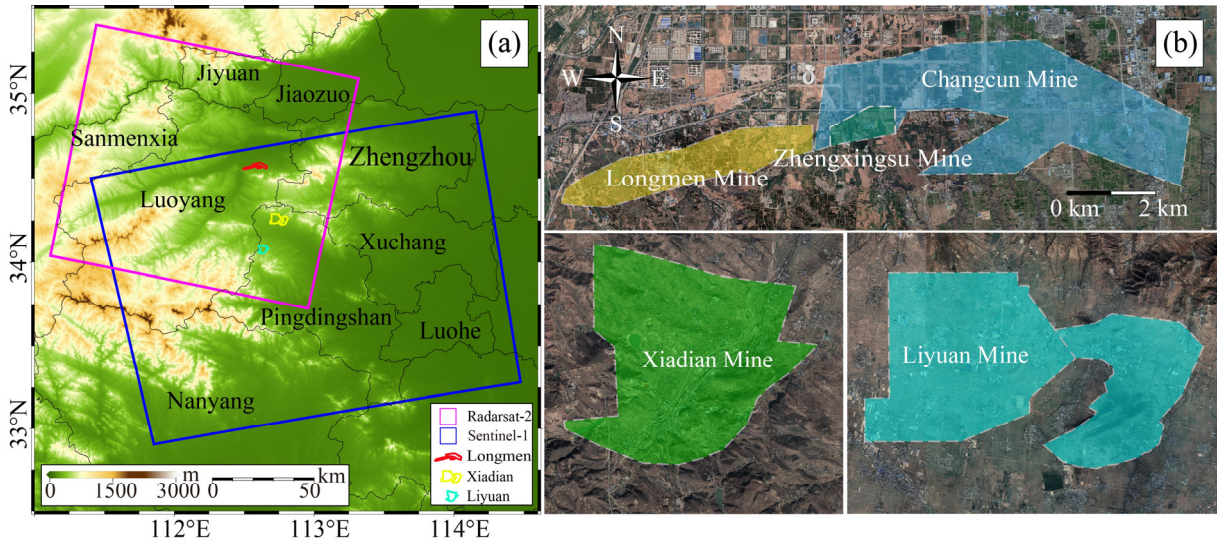

Figure 1. Study area and data coverage: (**a**) footprints of Radarsat-2 (pink) and Sentinel-1 (blue); (**b**) coverage of three studied mine areas.

2.2. InSAR Data Processing

This study utilized two types of SAR data (Table 1): (1) Radarsat-2 wide-mode data (11 images) acquired from 31 January 2012 to 10 January 2016; and (2) Sentinel-1A/B TOPS-mode data (190 images) acquired between 13 November 2015, and 30 December 2022, to monitor surface deformation throughout the entire life cycle of the mining areas.

Table 1. SAR data used in this study.

Sensor	Wavelength	Azimuth/Range Pixel Spacing	Orbit Direction	Path	Temporal Coverage
Sentinel-1	5.6 cm	13.94 m/2.33 m	Ascending	113	13 November 2015–30 December 2022
Radarsat-2	5.6 cm	5.22 m/11.84 m	Descending	21571L	31 January 2012–10 January 2016

We performed PS-InSAR data processing by differential interferometry, PS point selection, and time series estimation (Figure 2). We first selected the primary images to decrease the potential decorrelation by minimizing the temporal and spatial baselines. The 31 July 2014 and 8 January 2019 were selected to form interferogram stacks of Radarsat-2 and Sentinel-1, respectively (Figure 3a). The interferometric processing included registration, topography, and flat-earth phase removal, and interferogram generation was performed using the GAMMA software. We utilized the 1 arc-sec Shuttle Radar Topography Mission (SRTM) DEM (https://earthexplorer.usgs.gov, accessed on 5 April 2024) to remove topography and flat-earth phases. Precise orbits (https://qc.sentinel1.eo.esa.int, accessed on 5 April 2024) were used for orbital corrections to minimize the noise, and adaptive filtering was applied.Second, we selected the PS points by a two-step method to identify the reliable scatterers for the deformation estimation. We employed the amplitude dispersion thresholds $D_A = 0.42$ and $D_A = 0.6$ for SBAS for PS point and conducted slowly decorrelating filtered phase (SDFP) point detection. Subsequently, PS candidates were refined by the temporal coherence coefficient γ_k and the variation in phase residual. Here, the temporal coherence coefficient γ_k is defined as follows [8]:

$$\gamma_k = \frac{1}{N}\left|\sum_{i=1}^{N} \exp\left\{j\left(\phi^i_{\text{diff}} - \tilde{\phi}^i - \phi^{i,u}_{\theta,}\right)\right\}\right| \quad (1)$$

where ϕ^{i}_{diff} is the differential phase; $\tilde{\phi}^{i}$ is the spatially correlated phase; and $\phi^{i,u}_{\theta,}$ is the phase of the spatially uncorrelated look angle error. Then, the three-dimensional phase-unwrapping algorithm was applied to obtain the unwrapped phase $\varphi_{\mathrm{unw},x,i}$ for each high coherence point:

$$\varphi_{\mathrm{de},x,i} \approx \varphi_{\mathrm{unw},x,i} + \hat{\varphi}^{m}_{\mathrm{atm},x} - \hat{\varphi}^{s}_{\mathrm{atm},x,i} + \Delta\hat{\varphi}^{m}_{\mathrm{orb},x} - \Delta\hat{\varphi}^{s}_{\mathrm{orb},x,i} - \Delta\varphi^{\mathrm{corr}}_{\theta,x,i} - \Delta\varphi_{n,x,i} - 2k_{x,i}\pi \quad (2)$$

where $\varphi_{\mathrm{de},x,i}$ is the target deformation, $\hat{\varphi}^{m}_{\mathrm{atm},x}$ is the atmospheric screen in the primary image, and $\hat{\varphi}^{s}_{\mathrm{atm},x,i}$ is the atmospheric screen in the seceondary image; $\Delta\hat{\varphi}^{p}_{\mathrm{orb},x}$ and $\Delta\hat{\varphi}^{s}_{\mathrm{orb},x,i}$ represent the orbital error phases in the primary and secondary images, respectively; $\Delta\varphi^{\mathrm{corr}}_{\theta,x,i}$ denotes the noise associated with the residual spatial uncorrelation $\Delta\varphi_{n,x,i}$; and $2k_{x,i}\pi$ is the phase integer ambiguity.

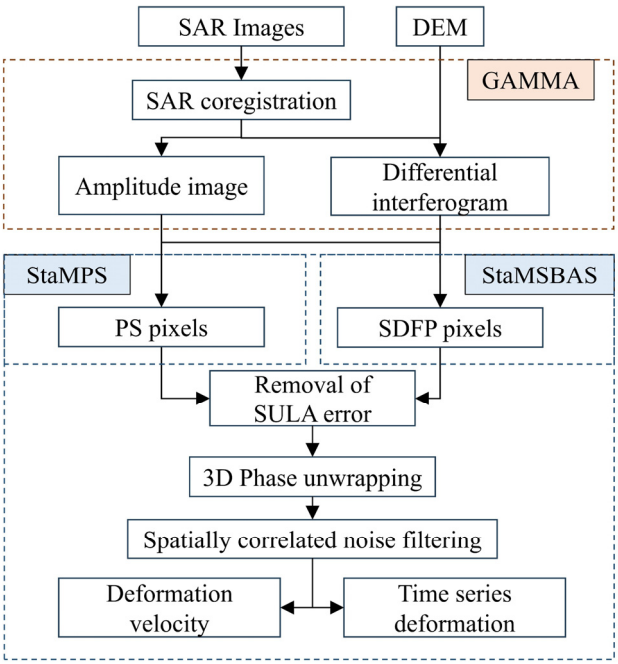

Figure 2. The flowchart of SAR data processing.

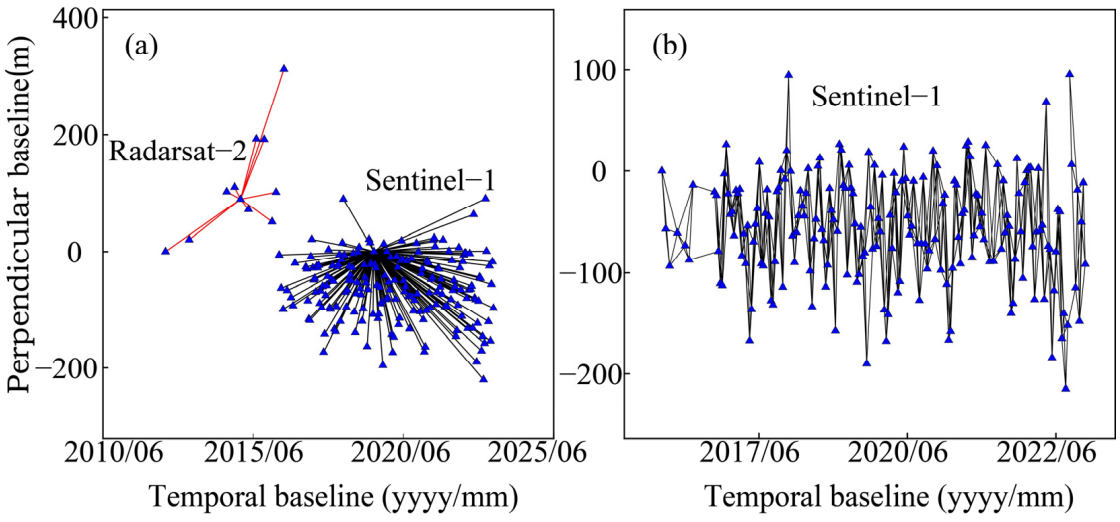

Figure 3. Baseline configurations of InSAR data: (**a**) PS baseline map; (**b**) SBAS baseline map.

The spatially correlated look angle (SCLA) error in the PS pixels of the interferograms is estimated after the phase unwrapping step. The SCLA error is estimated by applying a high pass filter in time and low pass filter in space to the unwrapped phase values. Finally, the SCLA error is subtracted from the remaining phase to obtain the deformation estimates.

Due to the lack of in situ measurements, this study assessed the reliability of the PS-InSAR results by a cross-validation with SBAS-InSAR [35,36]. For SBAS analysis, the maximum temporal and spatial baseline thresholds were set as 96 days and 150 m, respectively. The SBAS stacks contain 538 interferograms (see Figure 3b).

2.3. Deformation Modeling Based on Rectangular Model

To probe the geometry of coal mine production, we applied the Okada rectangular model and the Bayesian inversion method to the Xiadian area, which has been continuously exploited since January 2012. We first subsampled the InSAR velocities from 2012 to 2022 with the quadtree method, retaining a total of 697 data points, which greatly reduced the computational complexity. As the exploitation map is unknown, we used a horizontal rectangular sill with uniform opening to simulate surface deformation, equivalent to the total mining impact. Specifically, according to the dislocation theory in the half-space, the surface displacement field caused by the opening component can be expressed as follows [29]:

$$\begin{cases} u_x = -\frac{U_3}{2\pi}\left[\frac{q^2}{R(R+\eta)} - I_3 \sin^2\delta\right] \\ u_y = -\frac{U_3}{2\pi}\left[\frac{-\tilde{d}q}{R(R+\xi)} - \sin\delta\left\{\frac{\xi q}{R(R+\eta)} - \tan^{-1}\frac{\xi\eta}{qR}\right\} - I_1 \sin^2\delta\right] \\ u_z = -\frac{U_3}{2\pi}\left[\frac{\tilde{y}q}{R(R+\xi)} + \cos\delta\left\{\frac{\xi q}{R(R+\eta)} - \tan^{-1}\frac{\xi\eta}{qR}\right\} - I_1 \sin^2\delta\right] \end{cases} \quad (3)$$

where u_x, u_y, and u_z are the surface displacement in Cartesian coordinates caused by the opening component U_3; ξ and η are the coordinates of the particle on the fault plane; and I_1, I_2, and I_3 are the influence coefficients.

Assuming that the horizontal mining activity, the dip angle, strike-slip component, and dip-slip component can be simplified as $\delta \approx 0$, $U_1 = 0$, and $U_2 = 0$, respectively, the surface deformation (Equation (3)) can be simplified as follows [37,38]:

$$u_z = \frac{U_3}{2\pi}\left[\frac{\tilde{y}q}{R(R+\xi)} + \frac{\xi q}{R(R+\xi)} - \tan^{-1}\frac{\xi\eta}{qR}\right] \quad (4)$$

Second, we utilized the open-source Geodetic Bayesian Inversion Software (GBIS) to apply nonlinear inversion to the mining geometry [39]. It employs Bayesian inference to quantify the optimal parameters, and their uncertainties were estimated using the Markov chain Monte Carlo method (MCMC), which incorporated the Metropolis–Hastings algorithm [40]. Specifically, the probability of the parameters can be determined as follows:

$$p(\mathrm{m} \mid \mathrm{d}) = \frac{p(\mathrm{d} \mid \mathrm{m})p(\mathrm{m})}{p(\mathrm{d})} \quad (5)$$

where d is the data vector, m is the set of model parameters, $p(\mathrm{m} \mid \mathrm{d})$ is the likelihood function of m given d based on residuals between the data and the model prediction of the observations, $p(\mathrm{m})$ expresses the prior information (in the form of a prior joint PDF) of the model parameters, and the denominator is a normalizing constant that is independent of m.

Therefore, the uncertainty gives an indication of the confidence interval of the inverted parameters. Here, we also constrained the initial intervals of the target parameters, considering the range of the deformation area and the minging depth, as follows: length $\in [0, 5000]$ m, width and depth $\in [0, 2000]$ m. We performed 10^6 iterations and removed the first 2×10^4 iterations as the burn-in period because the starting samples may highly depend on initial parameter settings and may not represent the real posterior PDFs.

3. Results

3.1. Deformation in Longmen Area

The Longmen area, located east of the Longmen Grottoes, contains the Longmen mining area, Zhengxingsu mining area, and Changcun mining area (Figure 1). The InSAR data reveal a consistent away-motion in the satellite LOS direction from 2012 to 2016. The average deformation rates for Longmen, Zhengxingsu, and Changcun were 5 mm/year, 10 mm/year, and 8 mm/year, respectively (Figure 4). Correspondingly, the maximum cumulative deformations were 22.4 mm, 38.5 mm, and 34.1 mm. However, in the following period from 2016 to 2022, these mining areas exhibited different deformation characteristics (Figure 5). The Zhengxingsu mining area continued to subside at 2 mm/year, while the Changcun mining area uplifted at 12 mm/year (Figure 6b,c). Notably, the Longmen mining area underwent a complex deformation transition in July 2014, November 2017, and March 2021 (Figure 6a).

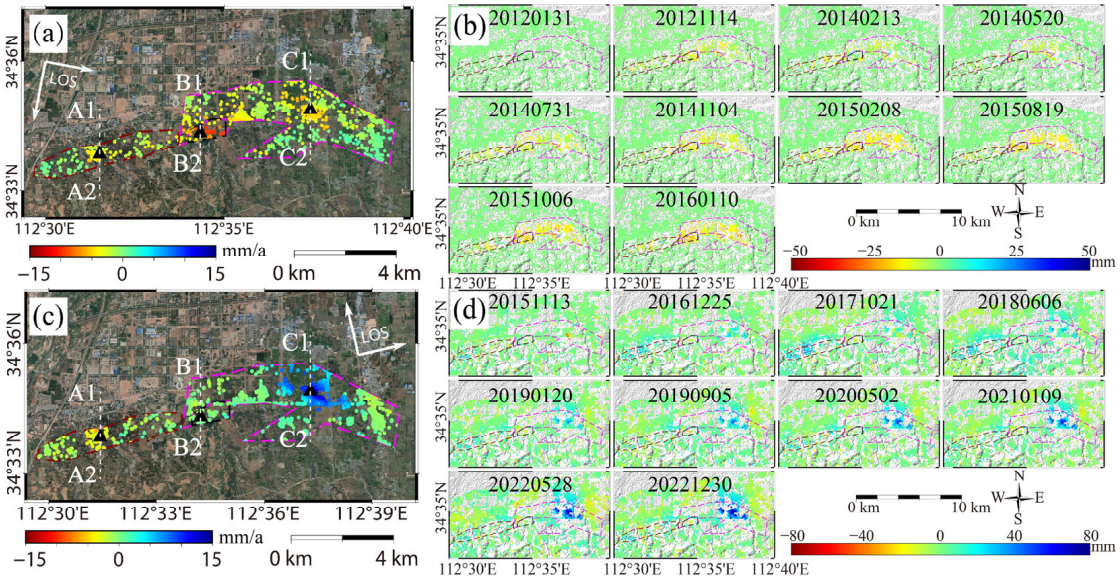

Figure 4. LOS deformation rate and cumulative deformation time series in the Longmen region from January 2012 to December 2022 from PS-InSAR: (**a**) LOS deformation rate obtained from Radarsat-2 data during 2012–2016; (**b**) time series of cumulative deformation from 2012 to 2016; (**c**) LOS deformation rate from Sentinel-1 during 2015–2022; and (**d**) time series of cumulative deformation from 2015 to 2022; A1-A2, B1-B2, and C1-C2 are the section lines drawn in Figure 5 (please note the different ranges of color bars in subplots for visualization).

To better describe the deformation evolution in the Longmen mining area, we selected the feature points P1-P3 and delineated the cross-profiles A1-A2, B1-B2, and C1-C2 (Figure 4). The Longmen mine area experienced three transition periods as subsidence at 10 mm/year from January 2012 to June 2014. Subsequently, from July 2014 to October 2017, the area underwent uplift at a rate of 4 mm/year. From November 2017 to February 2022, the mining area transformed to subsidence again, accruing a cumulative subsidence of approximately 22 mm. Subsequent to March 2022, the deformation reverted to uplift. However, there is only a single deformation transition within the Changcun mining area in September 2016, when a rate of 8 mm/year subsidence changed to a 12 mm/year uplift (Figures 5 and 6c). In contrast to the transition in the Longmen and Changcun mines, the Zhengxingsu mine experienced a two-stage subsidence, with a significant deceleration measured from 6 mm/year to 2 mm/year in June 2015 (Figures 5 and 6b).

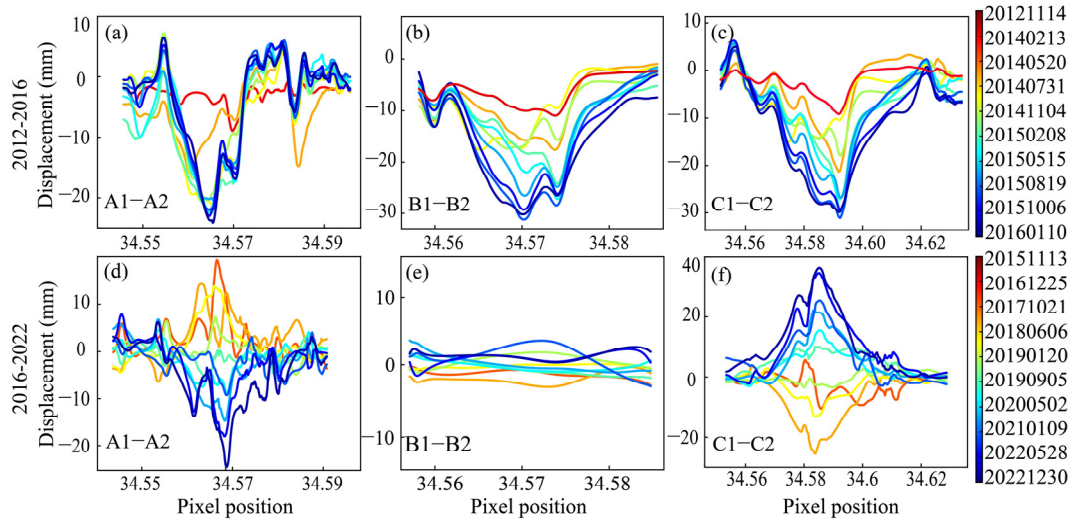

Figure 5. Cumulative deformation profiles A1-A2, B1-B2, and C1-C2 in Longmen mining area, Zhengxingsu mining area, and Changcun mining area. The location of the section lines A1-A2, B1-B2, and C1-C2 are shown in Figure 4: (**a**) A1-A2 in 2012–2016; (**b**) B1-B2 in 2012–2016; (**c**) C1-C2 in 2012–2016; (**d**) A1-A2 in 2016–2022; (**e**) B1-B2 in 2016–2022; and (**f**) C1-C2 in 2016–2022.

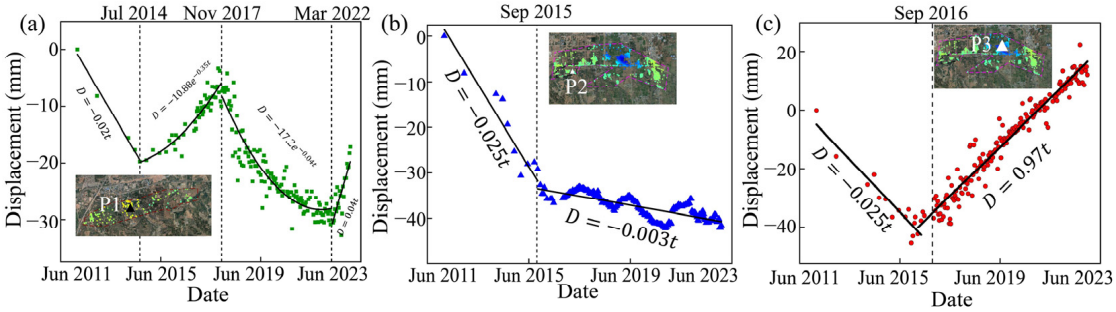

Figure 6. Time series deformation of selected points in Longmen area, the color-shaded areas are the average deformation rates of the mining areas: (**a**) Point P1 in Longmen area; (**b**) Point P2 in Zhengxingsu area; and (**c**) Point P3 in Changcun area.

3.2. Deformation in Xiadian Area

The Xiadian region, located in Xiadian Town, Ruzhou City, consists of two main deformation zones that cover 24.4 km^2. The InSAR result indicates that the Xiadian mining area has been steadily subsiding, with a maximum cumulative deformation of 10 cm (Figure 7).

Two notable deformation areas are Xiadian Town (Point P4) and Qianhu Town (Point P5) in the Xiadian area. In Xiadian town, the ground indicates a non-linear deformation, decreasing from 10 mm/year to 5 mm/year after 2016. However, the Qianhu area shows a continuous subsidence at 10 mm/year, resulting in a 10 cm cumulative deformation and the formation of the deformation profiles (D1-D2, E1-E2, G1-G2). It can be observed that the deformation area in the Xiadian mining area is extensive, with continuous subsidence over 10 years. The subsidence area covers approximately 25.86 km^2, and from 2016 to 2022, the cumulative deformation reached 50 mm (Figure 9). This resulted in a significant subsidence funnel with a width of approximately 3.1 km.

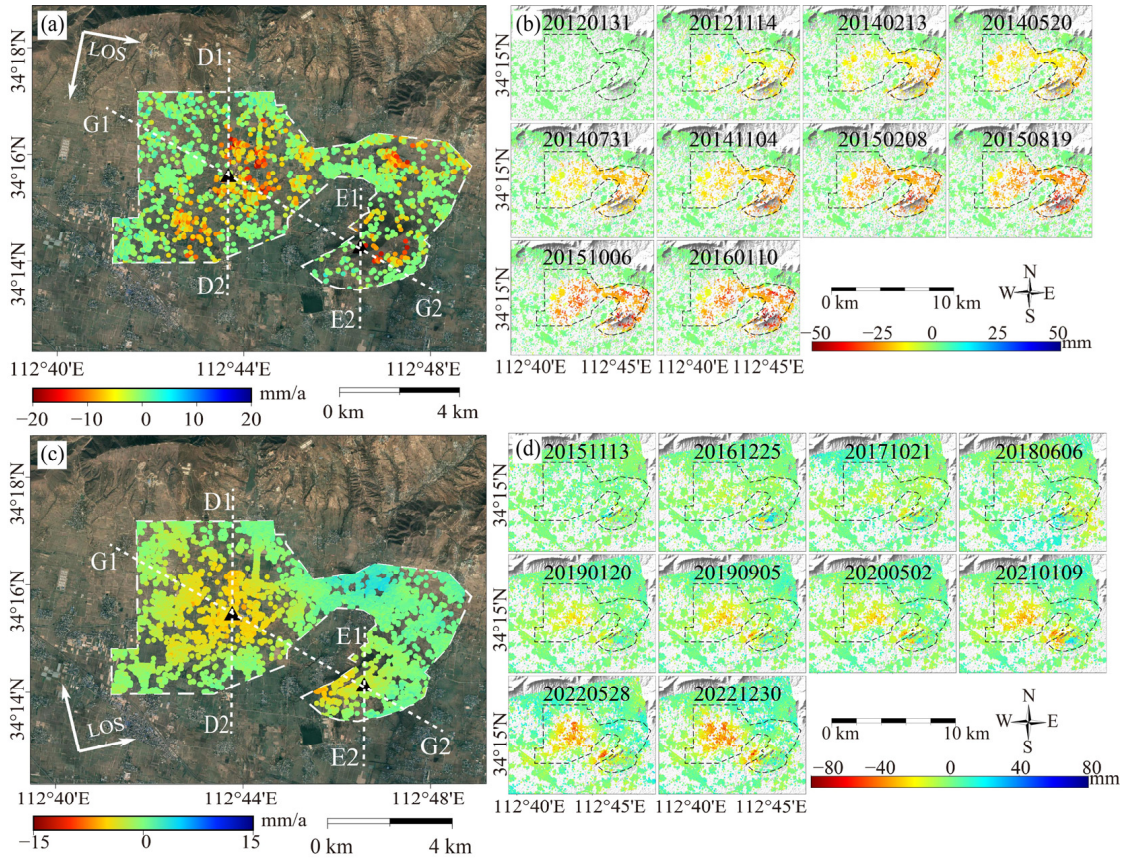

Figure 7. LOS deformation rate and cumulative deformation time series in the Xiadian region from January 2012 to December 2022 from PS-InSAR: (**a**) LOS deformation rate obtained from Radarsat-2 data during 2012–2016; (**b**) time series of cumulative deformation from 2012 to 2016; (**c**) LOS deformation rate from Sentinel-1 during 2015–2022; and (**d**) time series of cumulative deformation from 2015 to 2022; D1-D2, E1-E2, and G1-G2 are the section lines drawn in Figure 8 (please note the different ranges of color bars in subplots for visualization).

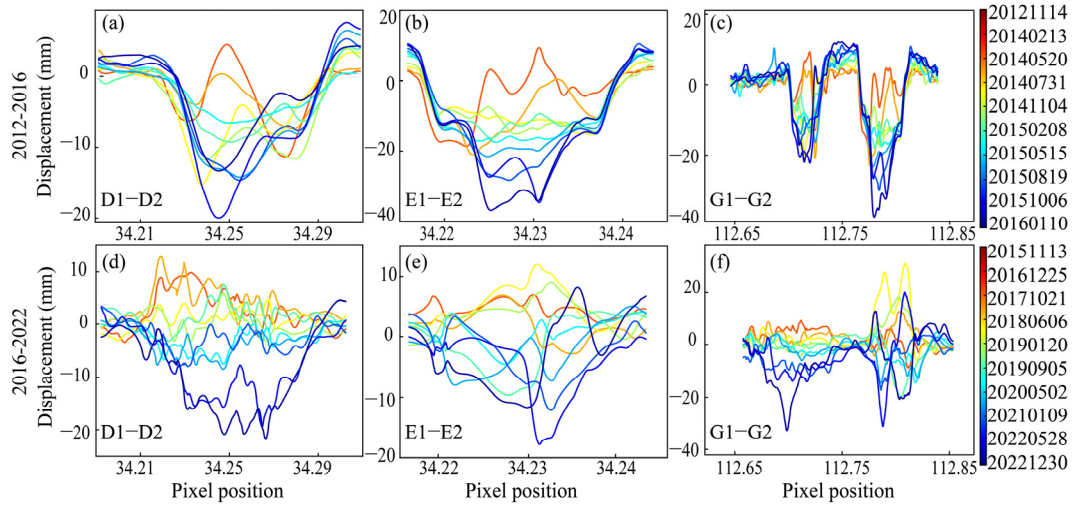

Figure 8. Cumulative deformation profiles D1-D2, E1-E2, and G1-G2 in Xiadian mining area. The location of section lines D1-D2, E1-E2, and G1-G2 are shown in Figure 7: (**a**) D1-D2 in 2012 to 2016; (**b**) E1-E2 in 2012–2016; (**c**) G1-G2 in 2012–2016; (**d**) D1-D2 in 2016–2022; (**e**) E1-E2 in 2016–2022; and (**f**) G1-G2 in 2016–2022.

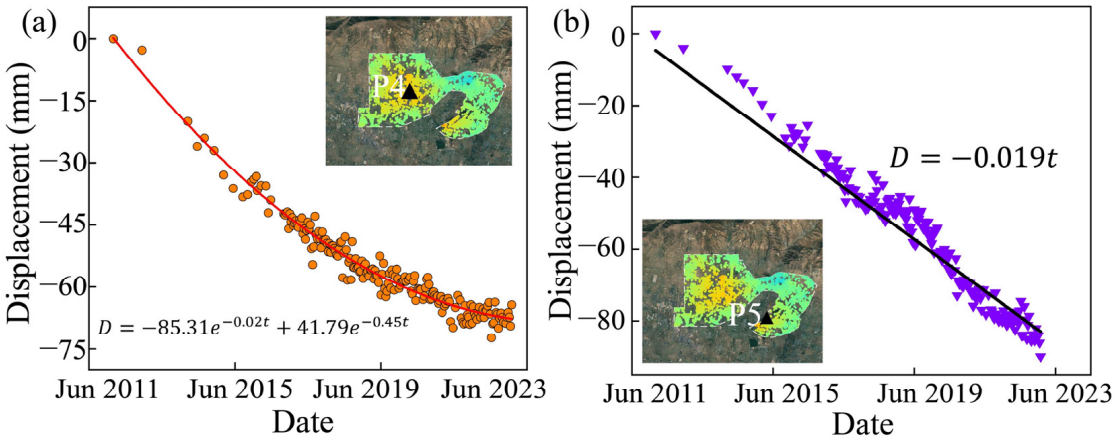

Figure 9. Time series deformation of selected points in Xiadian area, the color-shaded areas are the average deformation rates of the mining areas: (**a**) Point P4 in Xiadian mining area; (**b**) Point P5 in Xiadian mining area.

3.3. Deformation in Liyuan Area

Situated in the southwest of Ruzhou City, close to Jiliao Town, the Liyuan mining region covers an area of about 7 km^2. The mining area of Liyuan showed stable uplift deformation, with a maximum cumulative deformation of around 70 mm for the observation period of January 2012 to January 2016. Following that, a positive uplift deformation of between 5 and 10 mm/year was observed in the Liyuan mining area between November 2015 and December 2022 (Figure 10).

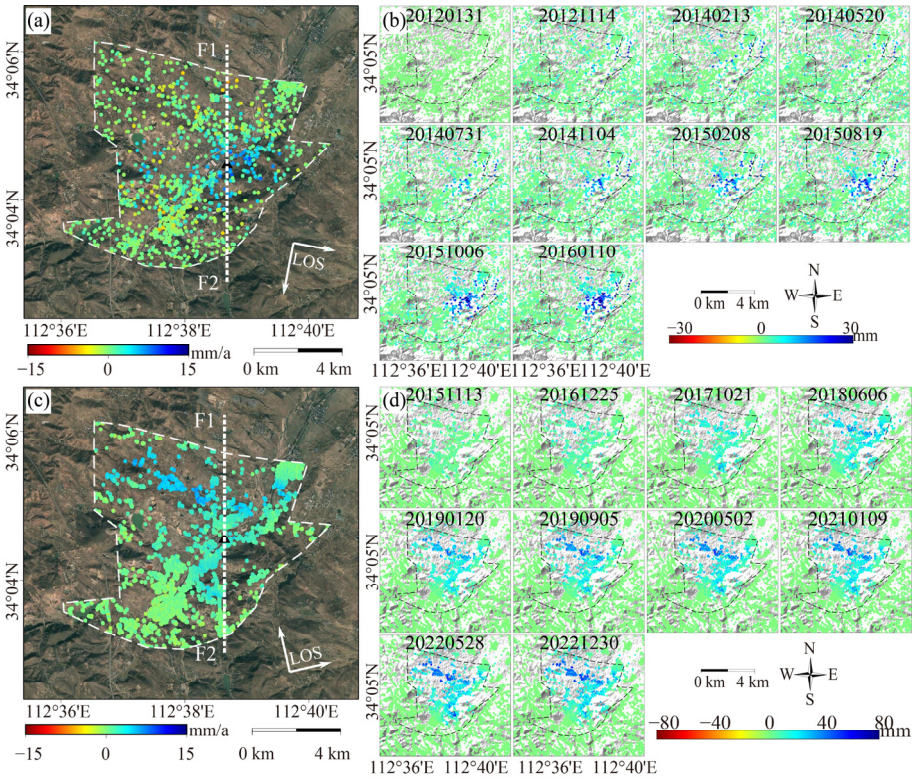

Figure 10. LOS deformation rate and cumulative deformation time series in the Liyuan region from January 2012 to December 2022 from PS-InSAR: (**a**) LOS deformation rate obtained from Radarsat-2

data during 2012–2016; (**b**) time series of cumulative deformation from 2012 to 2016; (**c**) LOS deformation rate from Sentinel-1 during 2015–2022; and (**d**) time series of cumulative deformation from 2015 to 2022; F1-F2 is the section line drawn in Figure 11 (please note the different ranges of color bars in subplots for visualization).

There is only one notable deformation area, which is Jiliao Town (Point P6) in the Liyuan area. The total uplift has reached 7 cm, with an average uplift rate of 5 mm/year. It is obvious that the uplift in the Liyuan mining area has a nonlinear characteristic, and the deformation has stabilized since December 2022. Specifically, from 2012 to 2013, the deformation rate was rather gradual. After 2014, it had a period of significant uplift, which continued until the deformation rate began to stabilize around 2020 (Figure 12).

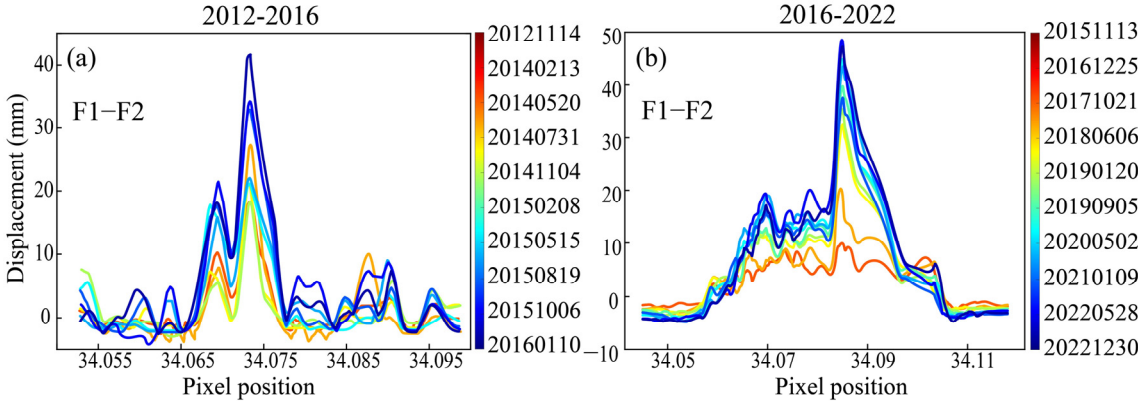

Figure 11. Cumulative deformation profile F1-F2 of Point P6 in Liyuan mining area; the location of section line F1-F2 is shown in Figure 10: (**a**) F1-F2 in 2012–2016; (**b**) F1-F2 in 2016–2022.

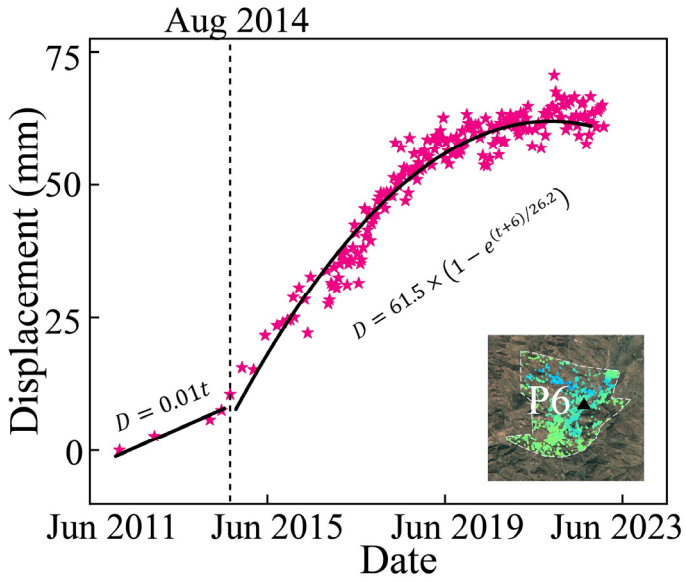

Figure 12. The time series deformation of the selected Point P6 in Liyuan area, the color-shaded area is the average deformation rate of the mining area.

3.4. Cross-Validation

To validate the reliability of the PS-InSAR results, we employed a cross-validation approach using PS and SBAS techniques in three mining areas (Figures 13–15). In Liyuan, Xiadian, and Longmen mining areas, the mean differences in deformation rates are 0.09 mm/year, 0.57 mm/year, and 0.65 mm/year, respectively. The standard deviations of these three areas are 0.98 mm/year, 1.5 mm/year, and 1.2 mm/year, with correlation coefficients of

0.82, 0.45, and 0.72, respectively. These good agreements from both methods confirms the reliability and accuracy of the derived deformation.

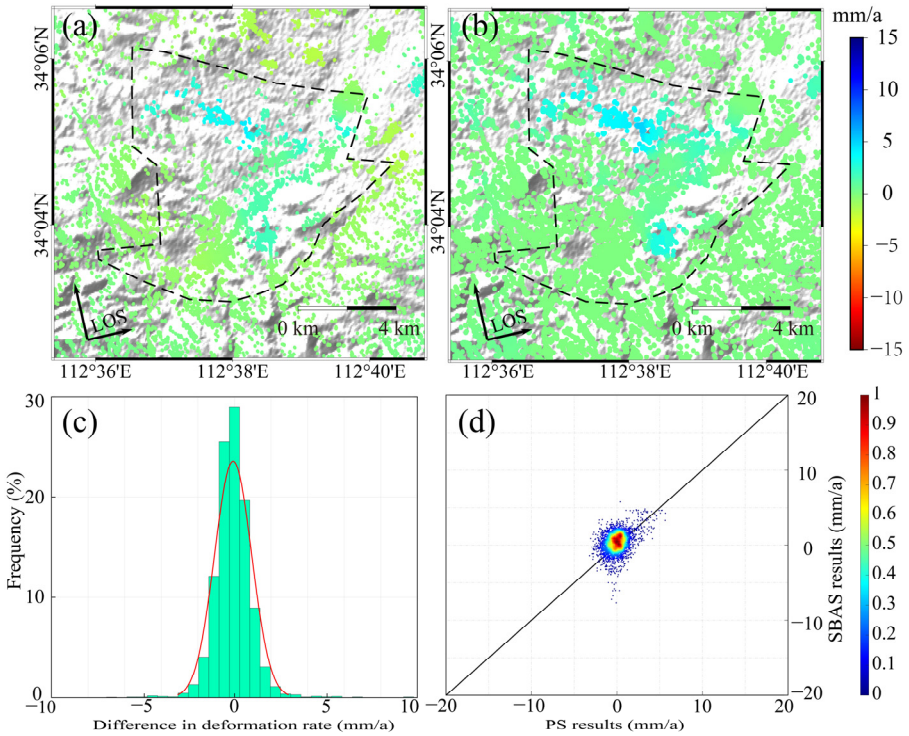

Figure 13. The cross-validation of InSAR results using PS and SBAS methods: (**a**) PS deformation rate in Liyuan mining area; (**b**) SBAS deformation rate in Liyuan mining area; (**c**) histogram of the difference between PS and SBAS; and (**d**) density scatter of two measurements.

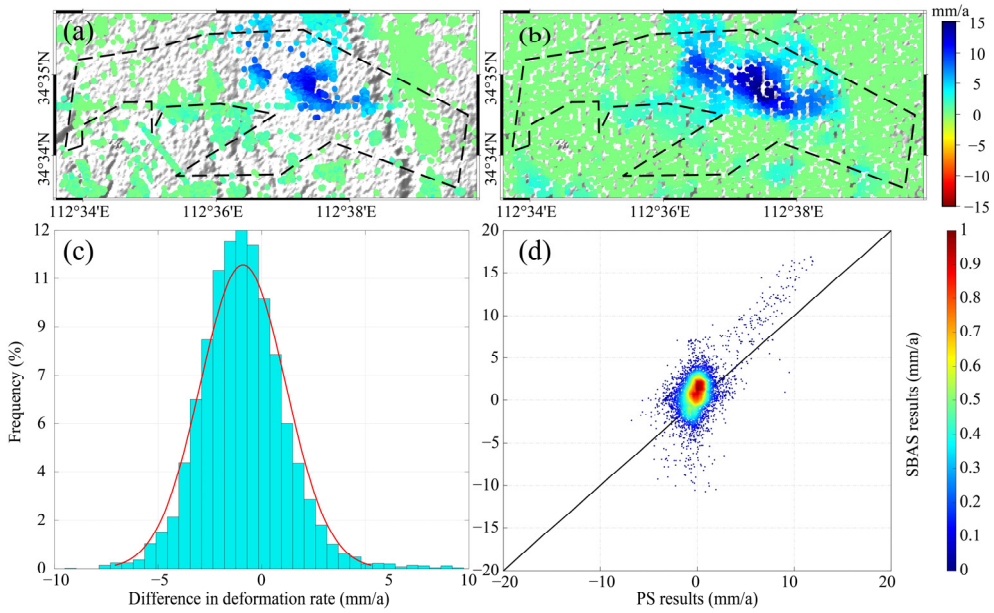

Figure 14. The cross-validation of InSAR results using PS and SBAS methods in Longmen area: (**a**) PS deformation rate in Longmen mining area; (**b**) SBAS deformation rate in Longmen mining area; (**c**) histogram of the difference between PS and SBAS in Longmen; and (**d**) density scatter of two measurements in Longmen.

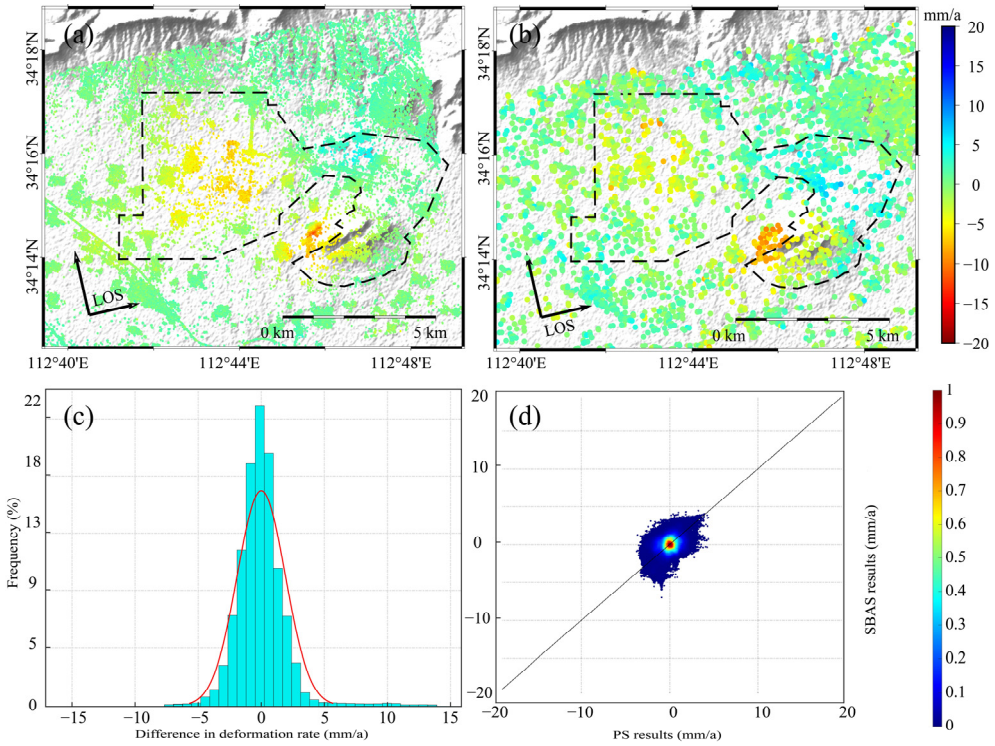

Figure 15. The cross-validation of InSAR results using PS and SBAS methods in Xiadian area: (**a**) PS deformation rate in Xiadian mining area; (**b**) SBAS deformation rate in Xiadian mining area; (**c**) histogram of the difference between PS and SBAS in Xiadian; and (**d**) density scatter of two measurements in Xiadian.

3.5. Modeling Parameters

We used the nonlinear Bayesian method to invert the mining geometry in the Xiadian area. The posterior PDFs of inverted parameters reveal that the sill geometry is well constrained after the 10^6 iterations (Figure 16). The overall distribution range of the residual results was [−5 cm, 5 cm], the mean residual value was 0.65 cm, and the standard deviation of the residuals was 1.79 cm, indicating that the surface simulation deformation results based on the Okada model had a high accuracy, and the inverted coal seam mining parameters were reliable (Figure 17c,d). The maximum posterior probability solution and 95% confidence intervals indicate the length, width, and depth of the mining tunnel and are 2634 ± 500 m, 309 ± 98 m, and 711 ± 290 m, respectively (Table 2). It has a SW-NE strike (254 ± 20°).

Table 2. Inverted parameters of mining geometry in Xiadian.

Model Parameters	Optimal Solution
Sill length (m)	$2634.43^{+336.40}_{-531.89}$
Sill width (m)	$309.01^{+97.70}_{-98.00}$
Sill depth (m)	$711.08^{+292.68}_{-110.74}$
Sill strike (deg)	$253.99^{+18.62}_{-20.62}$
Sill X (m)	$-167.54^{+188.57}_{-215.25}$
Sill Y (m)	$277.96^{+96.94}_{-98.94}$
Sill opening (m)	$-1.16^{+0.60}_{-0.58}$

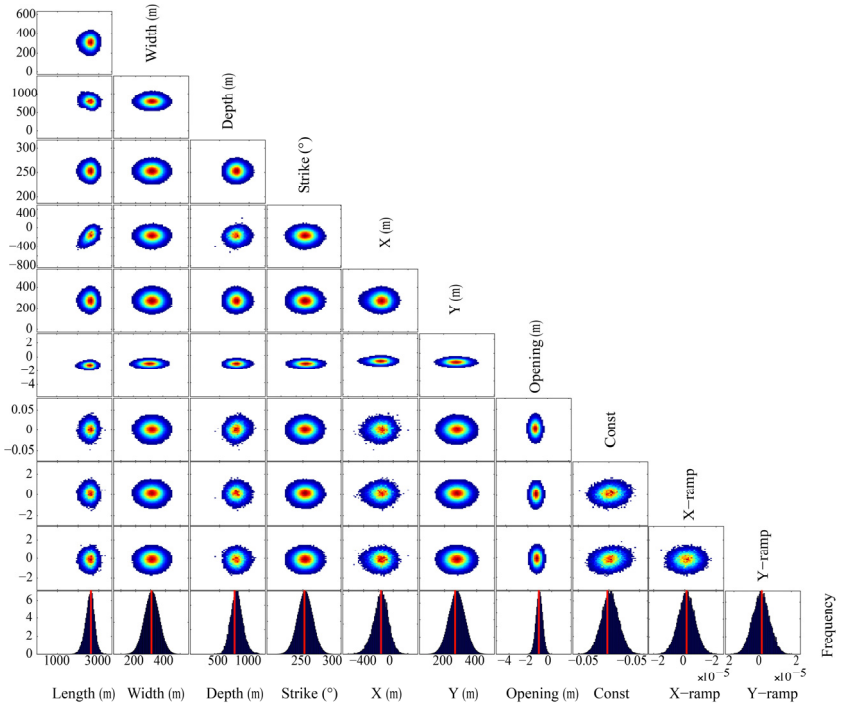

Figure 16. Posterior probability distributions of the mining geometry parameters.

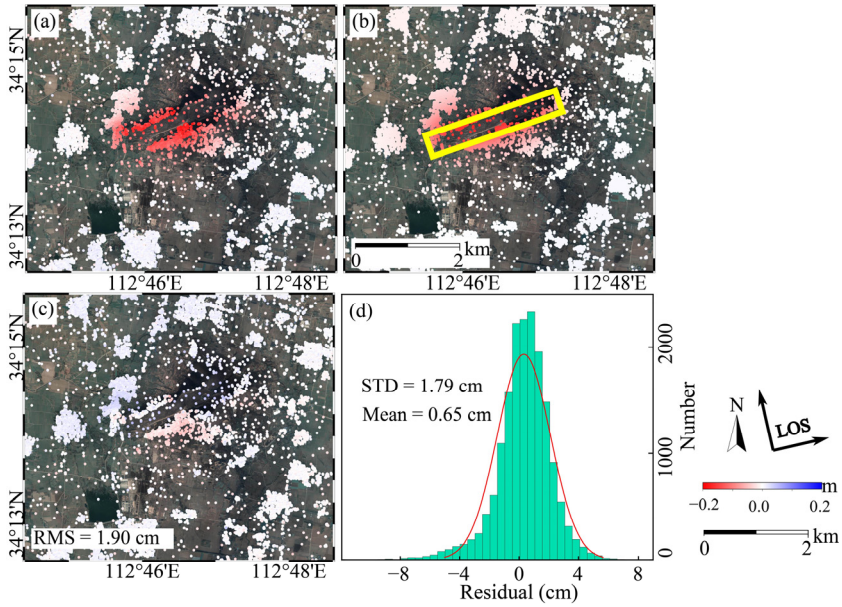

Figure 17. Comparison between InSAR observation and rectangular model in Xiadian mining area: (**a**) InSAR observation; (**b**) model prediction; (**c**) residual; and (**d**) histograms.

4. Discussion

This study investigated five mining areas using radar interferometry to comprehensively understand the life cycle stages of mining activities. The InSAR results revealed that the deformation patterns in continuously operated mining areas may undergo multiple transitions (e.g., Longmen mining area) or exhibit subsidence at varying rates (e.g., Zhengxingsu and Xiadian mining areas). After the closure, mine areas generally experience surface uplift, characterized by a linear or exponential function (e.g., Liyuan mining area).

4.1. The Possible Mechanisms for Deformation Transition in Mine Areas

We observed the transition of deformation in the Changcun and Longmen areas. First, in Changcun mine area, the single transition from subsidence to uplift on 14 September 2016 may be related to groundwater. As the groundwater was no longer extracted after the production ceased, the rising level of groundwater can directly result in the surface uplift. This phenomenon has also been observed in other closed mines, such as Limburg mine area in Germany [41]. Recently, Declercq et al. (2023) used Envisat data to map surface rebounds after the closure of the last active coal mine in Zolder, Belgium [42]. They demonstrated that the uplift transition in the western part of the mine can be attributed to the replenish of aquifer after the closure of mine. Similarly, Samsonov et al. (2013) found that after the cessation of the last exploitation at La Houve in Lorraine (French side) at the end of 2004 and the commencement of flooding in June 2006, the deformation reversed from subsidence to uplift [43]. Therefore, although the groundwater records are unavailable in Changcun mine area, according to the temporal development of the surface deformation, it is supposed that the process of groundwater recharge after the mine closure may cause the surface uplift. Complex spatiotemporal deformation characteristics also reveal different responses to surface deformation during different mining life cycles. In the Longmen mine, we observed two rounds of subsidence and uplift. The periods of subsidence from January 2012 to June 2014 and from November 2017 to February 2022 were mainly attributed to phased production activities [44]. Similar to the Changcun mine area, two phases of uplift in the Longmen mine area (i.e., July 2014–October 2017 and March 2022 to December 2022) may be related to the change in groundwater.

4.2. The Deformation Mechanism in Continuously Exploited Mines

The Xiadian mining area has been developed since 2010 and remained in continuous operation during our study period. The deformation is predominantly visible as linear subsidence. There are many factors that lead to mining area subsidence. The compaction of the goaf will drive the subsidence [45], and underground coal fires will also cause ground subsidence [46]. In our study, continuous mining caused a void beneath the surface and, finally, bending and subsiding of the overlying strata. The inverted parameters of the mining tunnel show a rectangular shape with a length of 2634 m, a width of 309 m, and a depth of 711 m.

4.3. The Deformation Mechanism in the Post-Closure Period

In contrast, the Liyuan mining area exhibits a significant difference to the Xiadian mining area. Throughout the 10-year monitoring period, the Liyuan mining area remained in a post-closure state. Following closure, the rising groundwater levels and changes in rock mass structure contributed to an uplift tendency. The uplifting velocity decays from 5 mm/year to 1 mm/year correspond to the exponential tendency of groundwater recovery in the post-closure areas [47].

5. Conclusions

This study utilized Sentinel-1 and Radarsat-2 interferometry to investigate long-term surface deformation across three mining areas in Luoyang and Pingdingshan from 2012 to 2022. We identified the deformation transitions in the Changcun and Longmen areas, which may be related to the rising groundwater after the mine closure and the levels of annual production. For the terminated Liyuan area, an equilibrium was reached, and the continuous uplift ceased in 2021. We also analyzed the mining tunnel in the Xiadian area, indicating a geometry with a depth of 711 m, width of 309 m, and length of 2634 m, with an opening of-1.2 m in the last decade. This study demonstrates the capability of long-term InSAR observations, especially for mining areas without available ground measurements, in deciphering the mine activities and facilitating small mining management throughout a mine's life cycle. In future, we suggest examining the impact of groundwater on mining activity by coupling hydro-mechanical models, well log data, and stratigraphic information.

Author Contributions: Conceptualization, X.Y., L.X. and W.D.; methodology, Z.M. and L.X.; investigation, Z.M. and L.X.; data curation, Z.M. and X.Y.; writing—original draft preparation, Z.M.; writing—review and editing, L.X., X.Y. and W.D.; visualization, Z.M.; funding acquisition, L.X. All authors have read and agreed to the published version of the manuscript.

Funding: This research was funded by the National Key Research and Development Program (2022YFB3903602), National Natural Science Foundation of China (42304037), Frontier Cross Research Project of Central South University (2023QYJC006), Hunan Province Dam Safety and Disease Prevention Engineering Research Center (Hndam2023kf05), and Natural Science Foundation of Hunan Province (2024JJ3031).

Data Availability Statement: The Sentinel-1A SAR images can be downloaded from the Alaska Satellite Facility (https://search.asf.alaska.edu/, accessed on 5 April 2024), and the precise orbit data (POD) can be obtained from the European Space Agency (http://aux.sentinel1.eo.esa.int/, accessed on 5 April 2024). The digital elevation model is from the United States Geological Survey (https://earthexplorer.usgs.gov/, accessed on 5 April 2024).

Acknowledgments: We are grateful to the editor and anonymous reviewers for reviewing the manuscript.

Conflicts of Interest: Author Wei Dong was employed by the company China Railway Siyuan Survey and Design Group Co., Ltd. The remaining authors declare that the research was conducted in the absence of any commercial or financial relationships that could be construed as a potential conflict of interest.

References

1. Liu, Q.; Wang, J.; Yang, K.; Di, S.; Dong, Z. Research on the model of accurate exploitation and utilization of underground space resources in closed/abandoned mines. *Coal Geol. Explor.* **2021**, *49*, 71–78.
2. Vervoort, A. Surface movement above an underground coal longwall mine after closure. *Nat. Hazards Earth Syst. Sci.* **2016**, *16*, 2107–2121. [CrossRef]
3. Chen, B.; Yu, H.; Zhang, X.; Li, Z.; Kang, J.; Yu, Y.; Yang, J.; Qin, L. Time-Varying Surface Deformation Retrieval and Prediction in Closed Mines through Integration of SBAS InSAR Measurements and LSTM Algorithm. *Remote Sens.* **2022**, *14*, 788. [CrossRef]
4. Zheng, M.; Zhang, H.; Deng, K.; Du, S.; Wang, L. Analysis of Pre- and Post-Mine Closure Surface Deformations in Western Xuzhou Coalfield From 2006 to 2018. *IEEE Access* **2019**, *7*, 124158–124172. [CrossRef]
5. Ma, F.; Sui, L.; Lian, W. Prediction of Mine Subsidence Based on InSAR Technology and the LSTM Algorithm: A Case Study of the Shigouyi Coalfield, Ningxia (China). *Remote Sens.* **2023**, *15*, 2755. [CrossRef]
6. Chen, Z.; Yang, Y.; Zhou, L.; Hou, H.; Zhang, Y.; Liang, J.; Zhang, S. Ecological restoration in mining areas in the context of the Belt and Road initiative: Capability and challenges. *Environ. Impact Assess. Rev.* **2022**, *95*, 106767. [CrossRef]
7. Ferretti, A.; Prati, C.; Rocca, F. Nonlinear subsidence rate estimation using permanent scatterers in differential SAR interferometry. *IEEE Trans. Geosci. Remote Sens.* **2000**, *38*, 2202–2212. [CrossRef]
8. Hooper, A.; Zebker, H.; Segall, P.; Kampes, B. A new method for measuring deformation on volcanoes and other natural terrains using InSAR persistent scatterers. *Geophys. Res. Lett.* **2004**, *31*, L23611. [CrossRef]
9. Berardino, P.; Fornaro, G.; Lanari, R.; Sansosti, E. A new algorithm for surface deformation monitoring based on small baseline differential SAR interferograms. *IEEE Trans. Geosci. Remote Sens.* **2002**, *40*, 2375–2383. [CrossRef]
10. Li, S.; Xu, W.; Li, Z. Review of the SBAS InSAR Time-series algorithms, applications, and challenges. *Geod. Geodyn.* **2022**, *13*, 114–126. [CrossRef]
11. Chen, Y.; Yu, S.; Tao, Q.; Liu, G.; Wang, L.; Wang, F. Accuracy Verification and Correction of D-InSAR and SBAS-InSAR in Monitoring Mining Surface Subsidence. *Remote Sens.* **2021**, *13*, 4365. [CrossRef]
12. Perski, Z.; Hanssen, R.; Wojcik, A.; Wojciechowski, T. InSAR analyses of terrain deformation near the Wieliczka Salt Mine, Poland. *Eng. Geol.* **2009**, *106*, 58–67. [CrossRef]
13. Chen, Y.; Dong, X.; Qi, Y.; Huang, P.; Sun, W.; Xu, W.; Tan, W.; Li, X.; Liu, X. Integration of DInSAR-PS-Stacking and SBAS-PS-InSAR Methods to Monitor Mining-Related Surface Subsidence. *Remote Sens.* **2023**, *15*, 2691. [CrossRef]
14. Kim, J.; Lin, S.-Y.; Singh, R.P.; Lan, C.-W.; Yun, H.-W. Underground burning of Jharia coal mine (India) and associated surface deformation using InSAR data. *Int. J. Appl. Earth Obs. Geoinf.* **2021**, *103*, 102524. [CrossRef]
15. Dai, S.; Zhang, Z.; Li, Z.; Liu, X.; Chen, Q. Prediction of Mining-Induced 3-D Deformation by Integrating Single-Orbit SBAS-InSAR, GNSS, and Log-Logistic Model (LL-SIG). *IEEE Trans. Geosci. Remote Sens.* **2023**, *61*, 5222213. [CrossRef]
16. Li, H.; Zheng, J.; Xue, L.; Zhao, X.; Lei, X.; Gong, X. Inversion of Subsidence Parameters and Prediction of Surface Dynamics under Insufficient Mining. *J. Min. Sci.* **2023**, *59*, 693–704. [CrossRef]
17. Dong, L.; Wang, C.; Tang, Y.; Tang, F.; Zhang, H.; Wang, J.; Duan, W. Time Series InSAR Three-Dimensional Displacement Inversion Model of Coal Mining Areas Based on Symmetrical Features of Mining Subsidence. *Remote Sens.* **2021**, *13*, 2143. [CrossRef]

18. Long, S.; Liu, M.; Xiong, C.; Li, T.; Wu, W.; Ding, H.; Zhang, L.; Zhu, C.; Lu, S. Research on Prediction of Surface Deformation in Mining Areas Based on TPE-Optimized Integrated Models and Multi-Temporal InSAR. *Remote Sens.* **2023**, *15*, 5546. [CrossRef]
19. Przyłucka, M.; Kowalski, Z.; Perski, Z. Twenty years of coal mining-induced subsidence in the Upper Silesia in Poland identified using InSAR. *Int. J. Coal Sci. Technol.* **2022**, *9*, 86. [CrossRef]
20. Wang, Z.H.; Wu, S.X.; Li, J.L.; Sun, W.C.; Wang, Z.F.; Liu, P.J. Surface subsidence and its reclamation of a coal mine locating at the high groundwater table, China. *Int. J. Environ. Sci. Technol.* **2023**, *20*, 13635–13654. [CrossRef]
21. Behera, A.; Singh Rawat, K. A brief review paper on mining subsidence and its geo-environmental impact. *Mater. Today Proc.* 2023; in press. [CrossRef]
22. Fadhillah, M.F.; Hakim, W.L.; Lee, S.-K.; Lee, K.-J.; Lee, S.-J.; Chae, S.-H.; Lee, H.; Lee, C.-W. Multitemporal analysis of land subsidence induced by open-pit mining activity using improved combined scatterer interferometry with deep learning algorithm optimization. *Sci. Rep.* **2024**, *14*, 6311. [CrossRef] [PubMed]
23. Guéguen, Y.; Deffontaines, B.; Fruneau, B.; Al Heib, M.; De Michele, M.; Raucoules, D.; Guise, Y.; Planchenault, J. Monitoring residual mining subsidence of Nord/Pas-de-Calais coal basin from differential and Persistent Scatterer Interferometry (Northern France). *J. Appl. Geophys.* **2009**, *69*, 24–34. [CrossRef]
24. Jung, H.C.; Kim, S.-W.; Jung, H.-S.; Min, K.D.; Won, J.-S. Satellite observation of coal mining subsidence by persistent scatterer analysis. *Eng. Geol.* **2007**, *92*, 1–13. [CrossRef]
25. Zhao, J.; Yang, X.; Zhang, Z.; Niu, Y.; Zhao, Z. Mine Subsidence Monitoring Integrating DS-InSAR with UAV Photogrammetry Products: Case Studies on Hebei and Inner Mongolia. *Remote Sens.* **2023**, *15*, 4998. [CrossRef]
26. Urrego, L.E.B.; Verstrynge, E.; Balen, K.V.; Wuyts, V.; Declercq, P.-Y. Settlement-induced damage monitoring of a historical building located in a coal mining area using PS-InSAR. In Proceedings of the 6th Workshop on Civil Structural Health Monitoring, Belfast, Ireland, 26–27 May 2016.
27. Gee, D.; Bateson, L.; Sowter, A.; Grebby, S.; Novellino, A.; Cigna, F.; Marsh, S.; Banton, C.; Wyatt, L. Ground Motion in Areas of Abandoned Mining: Application of the Intermittent SBAS (ISBAS) to the Northumberland and Durham Coalfield, UK. *Geosciences* **2017**, *7*, 85. [CrossRef]
28. Blachowski, J.; Jiránková, E.; Lazecky, M.; Kadlečík, P.; Milczarek, W. Application of satellite radar interferometry (PSINSAR) in analysis of secondary surface deformations in mining areas case studies from Czech Republic and Poland. *Acta Geodyn. Et Geomater.* **2018**, *15*, 173–185. [CrossRef]
29. He, L.; Cai, J.; Cao, W.; Mao, Y.; Liu, H.; Guan, K.; Zhou, Y.; Wang, Y.; Kang, J.; Wang, X.; et al. Comparative Analysis of Theoretical, Observational, and Modeled Deformation of Ground Subsidence: The Case of the Alhada Pb-Zn Mine. *Minerals* **2022**, *12*, 977. [CrossRef]
30. Okada, Y. Surface deformation due to shear and tensile faults in a half-space. *Bull. Seismol. Soc. Am.* **1985**, *75*, 1135–1154. [CrossRef]
31. Lu, Y.; Luo, Y. Using Linear and Nonlinear Inversion Algorithm Combined with Simple Dislocation Model Inversion of Coal Mine Subsidence Mechanism. *Int. J. Adv. Inf. Sci. Serv. Sci.* **2013**, *5*, 379–387.
32. Dai, Y.; Ng, A.H.M.; Wang, H.; Li, L.; Ge, L.; Tao, T. Modeling-Assisted InSAR Phase-Unwrapping Method for Mapping Mine Subsidence. *IEEE Geosci. Remote Sens. Lett.* **2021**, *18*, 1059–1063. [CrossRef]
33. Ren, W.; Jia, H.; Yan, B. Monitoring and parameter inversion of ground subsidence in mining area based on SBAS-InSAR method. *Bull. Surv. Mapp.* **2021**, 113–117+155. [CrossRef]
34. Miao, G.; Chen, Z. Analysis on Main Controlling Factors to Gas Occurrence in Changcun Coal Mine of Luoyang Longmen Coal Co., Ltd. *Zhongzhou Coal* **2013**, 11–13.
35. Hooper, A. A multi-temporal InSAR method incorporating both persistent scatterer and small baseline approaches. *Geophys. Res. Lett.* **2008**, *35*, L16302. [CrossRef]
36. Li, Y.-X.; Yang, K.-M.; Zhang, J.-H.; Hou, Z.-X.; Wang, S.; Ding, X.-M. Research on time series InSAR monitoring method for multiple types of surface deformation in mining area. *Nat. Hazards* **2022**, *114*, 2479–2508. [CrossRef]
37. Rongier, G.; Rude, C.; Herring, T.; Pankratius, V. Generative Modeling of InSAR Interferograms. *Earth Space Sci.* **2019**, *6*, 2671–2683. [CrossRef]
38. Steketee, J.A. Some Geophysical Applications of the Elasticity Theory of Dislocations. *Can. J. Phys.* **1958**, *36*, 1168–1198. [CrossRef]
39. Bagnardi, M.; Hooper, A. Inversion of Surface Deformation Data for Rapid Estimates of Source Parameters and Uncertainties: A Bayesian Approach. *Geochem. Geophys. Geosystems* **2018**, *19*, 2194–2211. [CrossRef]
40. Mosegaard, K.; Tarantola, A. Monte Carlo sampling of solutions to inverse problems. *J. Geophys. Res. Solid Earth* **1995**, *100*, 12431–12447. [CrossRef]
41. Caro Cuenca, M.; Hooper, A.J.; Hanssen, R.F. Surface deformation induced by water influx in the abandoned coal mines in Limburg, The Netherlands observed by satellite radar interferometry. *J. Appl. Geophys.* **2013**, *88*, 1–11. [CrossRef]
42. Declercq, P.-Y.; Dusar, M.; Pirard, E.; Verbeurgt, J.; Choopani, A.; Devleeschouwer, X. Post Mining Ground Deformations Transition Related to Coal Mines Closure in the Campine Coal Basin, Belgium, Evidenced by Three Decades of MT-InSAR Data. *Remote Sens.* **2023**, *15*, 725. [CrossRef]
43. Samsonov, S.; D'oreye, N.; Smets, B. Ground deformation associated with post-mining activity at the French–German border revealed by novel InSAR time series method. *Int. J. Appl. Earth Obs. Geoinf.* **2013**, *23*, 142–154. [CrossRef]

44. Yu, Z.; Huang, G.; Zhang, C. Monitoring and Characterization of Surface Deformation after the Closure of Coal Mines Based on Small Baseline Interferometric Synthetic Aperture Radar. *Instrum. Mes. Métrologie* **2020**, *19*, 141–150. [CrossRef]
45. Modeste, G.; Doubre, C.; Masson, F. Time evolution of mining-related residual subsidence monitored over a 24-year period using InSAR in southern Alsace, France. *Int. J. Appl. Earth Obs. Geoinf.* **2021**, *102*, 102392. [CrossRef]
46. Karanam, V.; Motagh, M.; Garg, S.; Jain, K. Multi-sensor remote sensing analysis of coal fire induced land subsidence in Jharia Coalfields, Jharkhand, India. *Int. J. Appl. Earth Obs. Geoinf.* **2021**, *102*, 102439. [CrossRef]
47. Whitworth, K.R. The monitoring and modelling of mine water recovery in UK coalfields. In *Mine Water Hydrogeology and Geochemistry*; Younger, P.L., Robins, N.S., Eds.; Geological Society of London: London, UK, 2002; Volume 198.